DE GRUYTER

Pure Appl. Chem. 2020; 92(3): 413–427

Conference paper

Robinson B. Dinamarca, Rodrigo Espinoza-González, Cristian H. Campos
and Gina Pecchi*

Magnetic Pt single and double core-shell structures for the catalytic selective hydrogenation of cinnmaladehyde

Abstract: This study reports the catalytic preparation, characterization, and evaluation of nanoscale core-shell structures with a γ-Fe_2O_3 core covered by a SiO_2 monoshell or by a $SiO_2@TiO_2$ multishell as a support for Pt nanoparticles (NPs) to synthesize active and operationally stable catalysts for selective liquid-phase cinnamaldehyde hydrogenation. The structures were designed with a magnetic core so they could be easily recovered from the catalytic bed by simple magnetization and with a SiO_2 monoshell or a $SiO_2@TiO_2$ multishell to protect the magnetic core. At the same time, this study details the effect of the shell on the catalytic performance. Moreover, the effect of particle size on the selective production of cinnamyl alcohol was studied by preparing two families of catalysts with metal loadings of 1 wt% and 5 wt% Pt with respect to the core-shell. The particle size effect enabled the $Fe_2O_3@SiO_2$-5%Pt system, with an average particle size of 5.6 nm, to reach 100 % conversion of cinnamaldehyde at 300 min of reaction, producing cinnamyl alcohol with 90 % selectivity; this result differed greatly from that of the $Fe_2O_3@SiO_2$-1%Pt ($d_{Pt} = 3.5$ nm) system, which reached a maximum conversion at 600 min with 49 % selectivity for the product of interest. However, the $Fe_2O_3@SiO_2@TiO_2$-x%Pt systems showed lower levels of conversion and selectivity compared to those of the $Fe_2O_3@SiO_2$-x%Pt catalysts, which is attributed to the fact that average metal particle sizes below 5.0 nm were obtained in both cases. After reduction in H_2 at 773 K, the $Fe_2O_3@SiO_2@TiO_2$-1%Pt catalyst showed deactivation, reaching 10 % conversion at 600 min of reaction and 60 % selectivity for the product of interest. However, the reduced $Fe_2O_3@SiO_2@TiO_2$-5%Pt system showed 98 % conversion with 95 % selectivity for cinnamyl alcohol at 24 h of operation; the increase in selectivity is attributed to the combined effects of the increase in average particle size (~7.5 nm) and the presence of strong metal-support interaction – SMSI – effects after reduction. Finally, the most selective systems were tested for operational stability, where the $Fe_2O_3@SiO_2@$-5%Pt catalyst could be reused in three consecutive operating cycles while maintaining its activity and selectivity for cinnamyl alcohol – unlike the $Fe_2O_3@SiO_2@TiO_2$ 5%Pt reduced system, which was deactivated after the third reaction cycle due to active phase leaching.

Keywords: core-shell materials; Eurasia 2018; heterogeneous catalysis; hydrogenations; platinum.

*Corresponding author: Gina Pecchi, Departamento de Físico-Química, Facultad de Ciencias Químicas, Universidad de Concepción, Edmundo Larenas 129, Concepción, Chile; and Millenium Nuclei on Catalytic Processes towards Sustainable Chemistry (CSC), Concepción, Chile, e-mail: gpecchi@udec.cl
Robinson B. Dinamarca and Cristian H. Campos: Departamento de Físico-Química, Facultad de Ciencias Químicas, Universidad de Concepción, Edmundo Larenas 129, Concepción, Chile
Rodrigo Espinoza-González: Department of Chemical Engineering, Biotechnology and Materials, FCFM, Universidad de Chile, Beauchef 851, Santiago, Chile

Introduction

Nanotechnology is a multidisciplinary field that has brought great advances in different areas such as medicine, biology, electronics, and catalysis [1–3]. Core-shell nanoparticles (CSNs) stand out among nanostructured materials because of their great impact on catalysis. CSNs consist of a core enveloped by one or more layers, in other words, a multifunctional system integrated into a single unit [4]. The catalytic performance of these structures depends to a great extent on the material composition and design, offering an improved nanoarchitecture resulting from the synergy that can be promoted between the core and shell or from the combination of the properties of the structural components [5].

CSNs have recently been examined as catalysts based on noble metals such as Ir, Pt, Ru, and Pd for the hydrogenation of α,β-unsaturated aldehydes to produce the respective α,β-unsaturated alcohols in a selective manner [6–15]. These molecules are used as building blocks to produce compounds of interest in fine chemistry. Among potential reactants, cinnamaldehyde (CIN) has been used as a test substrate in selective hydrogenation since it has three reactive centers: (i) the aromatic ring, (ii) the carbonyl group, and (iii) the C=C bond, as shown in Scheme 1. The literature has reported that the hydrogenation of CIN follows a Horiuti-Polanyi mechanism operating through adsorbed di-σ_{C-O} η^2, di-$\sigma_{C=C}$ η^2 and/or di-π η^2 states [16]. Therefore, given the competitive adsorption of C=C and C=O bonds on metal surfaces, a decrease in the interaction energy of the C=C bond with the metal surface is required to increase the selectivity for cinnamyl alcohol (COL) formation. The above has been achieved by including selectivity promoters capable of generating a strong metal-support interaction (SMSI) effect [17, 18]. The SMSI effect is observed in metals interacting with partially reducible oxides that, when prepared in a reducing atmosphere at temperatures above 300 °C, partially cover the metallic phase, promoting C=O catalytic hydrogenation performance. Nevertheless, most of these studies have reported on metal-based catalysts supported by micrometer-sized materials such as TiO_2 [19–23], CeO_2 [20, 24], and ZnO [21, 25], among others.

Another effect studied in the selective production of COL has been that of the particle size of the active phase, especially for Pt and Ru [26–31]. Recently, Durndell et al. reported an increase in the selective production of COL with metal crystal sizes above 3.0 nm in Pt/SiO_2 and Pt/SBA-15 catalysts [27]. The authors attributed this behavior to increased repulsive interactions between the electron density of the phenyl group and that of the metal surface with increases in the active-phase crystal size. Furthermore, Plomp et al. reported a study on the effect of Pt crystal size in heat-treated carbon-nanofiber (CNF)-supported systems where preferential adsorption of the phenyl group on the surface of the deoxygenated support (nonpolar support) favored the hydrogenation of the C=O group, even on Pt nanoparticles (NPs) with an average size of 1.8 nm [29].

Both effects have resulted in selective systems for the semi-hydrogenation of CIN to produce COL as the main product. However, only some studies have reported using active, selective, easily recoverable, and operationally stable CSNs for this reaction. This study suggests the preparation of Pt catalysts with a CSN architecture to investigate the effects of (1) incorporating TiO_2 as a partially reducible oxide at the nanoscale, (2) the Pt particle size, and (3) the reduction temperature for the selective hydrogenation of CIN using the
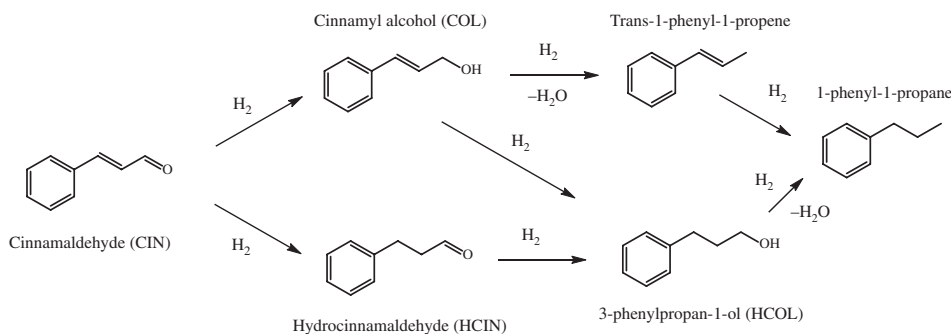
Scheme 1: Hydrogenation pathways for CIN.

shell-TiO_2 system. The catalysts were designed to obtain CSN systems with a magnetic core to allow for separation from the reaction bed by magnetization and with a SiO_2 monoshell or a SiO_2@TiO_2 multishell to protect the core during catalysis, as well as to serve as a support to immobilize Pt NPs. The catalysts were prepared in consecutive steps using a Fe_3O_4 magnetic core enveloped with SiO_2 (FS) in the first step. A second TiO_2 shell (FST) was incorporated into the FS system using a Stöber-like method. Both systems were calcined at 500 °C, and then four FS-Pt(x) and FST-Pt(x) supported catalysts were prepared, where x = 1.0 % or 5.0 %. To evaluate the SMSI effect, the FST-Pt(x) systems were reduced in hydrogen at 773 K. The most selective catalysts of each family were subjected to consecutive operating cycles to evaluate their operational stability.

Experimental

Synthesis of Fe_3O_4 nanoparticles NPs

Fe_3O_4 NPs were synthesized by a solvothermal method following Long et al. [6]. $FeCl_3$ (Merck®) was dissolved in a polyvinyl pyrrolidone (PVP K30, Sigma®) solution in ethylene glycol (EG, Merck®). The mixture was transferred to a Teflon autoclave and isothermally treated at 473 K for 12 h. The solid obtained was separated by magnetization and washed several times with absolute ethanol.

Synthesis of Fe_3O_4@SiO_2 (FS) and Fe_3O_4@SiO_2@TiO_2 (FST)

Fe_3O_4-core NPs were coated with SiO_2 using the Stöber method [6]. Fe_3O_4 NPs were dispersed in a mixture of ethanol, water, and ammonia, and tetraethyl orthosilicate (TEOS, Merck®) was slowly added to the dispersion under stirring for 6 h. The Fe_3O_4@SiO_2 solid was separated by magnetization and washed several times with an ethanol-water mixture. A second coating of TiO_2 was deposited on the FS surface by a modified Stöber method using titanium butoxide (TBOT, Sigma®) as a precursor [32], producing the Fe_3O_4@SiO_2@TiOOH system. Finally, the Fe_3O_4@SiO_2 and Fe_3O_4@SiO_2@TiOOH systems were calcined from room temperature to 773 K at a heating rate of 5 K/min in static air, obtaining the Fe_2O_3@SiO_2 (FS) and Fe_3O_4@SiO_2@TiO_2 (FST) materials, as shown by X-ray diffraction (XRD) (see below).

Synthesis of FS-Pt(x) and FST-Pt(x) catalysts

The catalysts were synthesized by surface deposition with the help of a coupling agent to promote active phase immobilization and dispersion on the surface of the material [33]. The FS and FST surfaces were functionalized with (3-aminopropyl)trimethoxysilane (AMPTS, Merck®, 1 mL/g of solid) by refluxing in toluene for 24 h under mechanical stirring. Finally, the solid was separated by magnetization, washed with a toluene-acetone mixture, and dried in an oven at 323 K for 12 h.

The material obtained was dispersed in a K_2PtCl_6 (Merck®) solution with an amount of precursor necessary to produce 1.0 wt% systems with respect to FS and FST. The materials were placed into contact with the solution for 3 h under mechanical stirring and then reduced with a fresh solution of $NaBH_4$ (Merck®). The obtained systems were listed as FS-Pt(1) and FST-Pt(1). A sequential impregnation-reduction method was used to produce 5.0 wt% Pt systems. In general, the procedure described for the 1 wt% synthesis was repeated five consecutive times, reducing the $PtCl_4^{2-}$ precursor between each impregnation.

To evaluate the SMSI effect, the catalyst was reduced ex situ in H_2 at a flow of 30 mL/min while heating the system at a rate of 5 °/min from room temperature to 773 K and maintaining it at that temperature for 1 h. The system was cooled in H_2 to room temperature and purged with N_2 for 30 min before catalyst evaluation.

Characterization

The morphology and microanalysis of the structures were studied by scanning transmission electron microscopy with energy dispersive X-ray spectroscopy (STEM-EDS) using an FEI Tecnai ST F20 microscope operating at 200 kV. Adsorption isotherms were obtained at 77 K in a Micromeritics ASAP 2010 instrument. X-ray powder diffraction profiles were obtained in a Rigaku Diffractometer with Cu K_α radiation ($\lambda = 1.5418$ Å) and a nickel filter. Fourier transform infrared (FTIR) spectra were obtained with a Nicolet Magna-IR 550 spectrometer. The reduction profiles of the prepared systems were obtained by a Micromeritics temperature-programed reaction/desorption (TPR/TPD) 2900 instrument equipped with a thermal conductivity detector while performing the experiments in a 40 mL min^{-1} flow of a 5 % H_2/Ar mixture from room temperature to 1073 K. The magnetic behavior was studied using a Lakeshore series 7400 vibrating sample magnetometer (VSM) in an applied field of 20 kOe at 300 K. The Pt and Fe contents were determined by inductively coupled plasma – optical emission spectroscopy (ICP-OES) with a Perkin-Elmer Optima 2100 DV instrument. The catalyst contents were determined after digestion in a 1:3 mixture of HNO_3:HCl. To assess Pt leaching, the supernatant fluid was measured once the reaction was finished. X-ray photoelectron spectroscopy (XPS, RQ-300 X-ray Source, STAIB Instruments) was performed to determine the binding energies of the samples using Al radiation ($h\nu = 11486.6$ eV) operated at 75 W.

Catalytic activity

The catalytic activity for CIN hydrogenation was evaluated in a Parr® 5513 reactor equipped with a temperature controller and mechanical stirring. The operating conditions used ensured only kinetic control during the catalytic performance evaluation [34]. A catalyst amount of 0.030 g was used to reach a molar ratio of $n_{CIN}/n_{Pt} = 600$, using 25 mL of cyclohexane as solvent, a P_{H2} of 20 bar, and a temperature of 373 K. Noninvasive samples (25–50 μL) were extracted from the reactor and analyzed in an HP 4890D gas chromatograph equipped with an HP-5 semicapillary column and a flame ionization detector (FID). All products were followed based on commercial standards (Sigma®). The conversion and selectivity were calculated using calibration curves and the following equations:

$$X_{CIN}(\%) = \frac{[CIN]_i - [CIN]_t}{[CIN]_i} \cdot 100 \tag{1}$$

$$S_{product}(\%) = \frac{[product]_t}{[CIN]_i - [CIN]_t} \cdot 100 \tag{2}$$

Recycling tests were performed to evaluate the operational stability of the catalysts. The catalyst was magnetically separated from the catalytic bed, and 50 mL of cyclohexane and the amount of CIN required to repeat the reaction were added consecutively. This operation was repeated two times in succession. After the first cycle, the catalyst was also separated from the reaction medium, and the hydrogenation was continued to evaluate the leaching of the active phase.

Results and discussion

Characterization of supports and catalysts

The FS and FST systems were surface modified with APTMS to promote the immobilization of $PtCl_4^{2-}$ on the surface [33]. Figure 1 displays the FTIR characterization of the modified materials, where all systems show the characteristic bands associated with Fe−O−Fe bonds at 580 cm^{-1} and Si−O−Si bonds (asymmetric
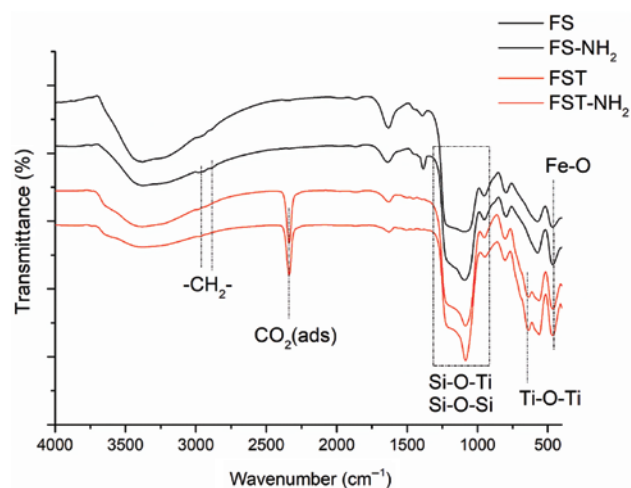
Fig. 1: FTIR characterization for the modified FS and FST supports.

v_{as}Si–O–Si and symmetric v_sSi–O–Si stretching modes at 964 cm^{-1} and 1100 cm^{-1}, respectively) [35]. The TiO$_2$-shell system presents a low-intensity band at 610 cm^{-1} attributed to the vibration of Ti–O–Ti species and a clear band at 2350 cm^{-1} attributed to the asymmetric vibration of CO$_2$ adsorbed on TiO$_2$ [13]. Furthermore, the bands attributed to the vibration of –CH$_2$ groups at 2900 cm^{-1} are shown in Fig. 1. For the FS and FST systems, the signals at 3400–3500 cm^{-1} and 1646 cm^{-1} are attributed to the OH stretching vibrations and H–O–H bending of the Si–OH or Ti–OH groups and physisorbed H$_2$O, respectively [35]. By incorporating APTMS, a decrease in the intensity of the Si–OH and Ti–OH vibrations is detected and attributed to the immobilization via the formation of (Si–O)$_x$–Si(OCH$_3$)$_{3-x}$(CH$_2$)$_3$NH$_2$ or (Ti–O)$_x$–Si(OCH$_3$)$_{3-x}$(CH$_2$)$_3$NH$_2$, in line with reports by Deepti et al. [36].

The catalysts were characterized by ICP-OES to determine the Pt content, as summarized in Table 1. The FS-Pt(x) catalysts contain Pt contents lower than the nominal values, while the FST-Pt(1) and FST-Pt(5) catalysts yield values of 1.1% Pt and 5.3% Pt, respectively. The differences in metal charges are attributed to the interactions of each system observed during immobilization, as outlined in Scheme 2. The measured zeta potentials of the particles, as included in Table 1, reveal that the FS system has a negative surface charge (ZPC=–11.3 mV) when dispersed in water, suggesting that the deposition of the PtCl$_4^{2-}$ precursor on the surface of the material occurs by interaction with the immobilized –NH$_2$ group (pKa=10.6) [37]. In contrast, the FST system has a positive surface charge (ZPC=23.7 mV), which could promote the interaction of the

Table 1: ICP-OES, ZPC, S$_{BET}$ HR-TEM characterization for the as synthetized supports and catalysts based on FS and FST materials.

Material	Pt content[a] (%)	ZPC (mV)[b]	S$_{BET}$ (m²/g)	Core mean diameter (nm)	Thickness mean diameter (nm)		Pt mean diameter (nm)	D$_{TEM}$[c]
					SiO$_2$	TiO$_2$		
FS	–	–11.3 (6.6)	11	229±75	50±10	–	–	–
FS-Pt(1)	0.7 (1.0)	–	11	248±77	42±12	–	3.6±1.0	32.1
FS-Pt(5)	3.5 (5.0)	–	10	238±70	43±14	–	5.4±1.5	21.4
FST	–	23.7 (6.5)	20	221±65	52±4	14±7	–	–
FST-Pt(1)	1.1 (1.0)	–	11	250±81	59±5	14±5	2.9±0.5	39.9
FST-Pt(5)	5.3 (5.0)	–	9	237±74	55±7	16±8	4.9±0.5	23.6

[a]Nominal values in brackets. [b]pH of the dispersion in brackets. [c]The dispersion was calculated assuming spherical particles, by the expression $D=\dfrac{1.157}{d(nm)}\cdot 100$ extracted from [39].
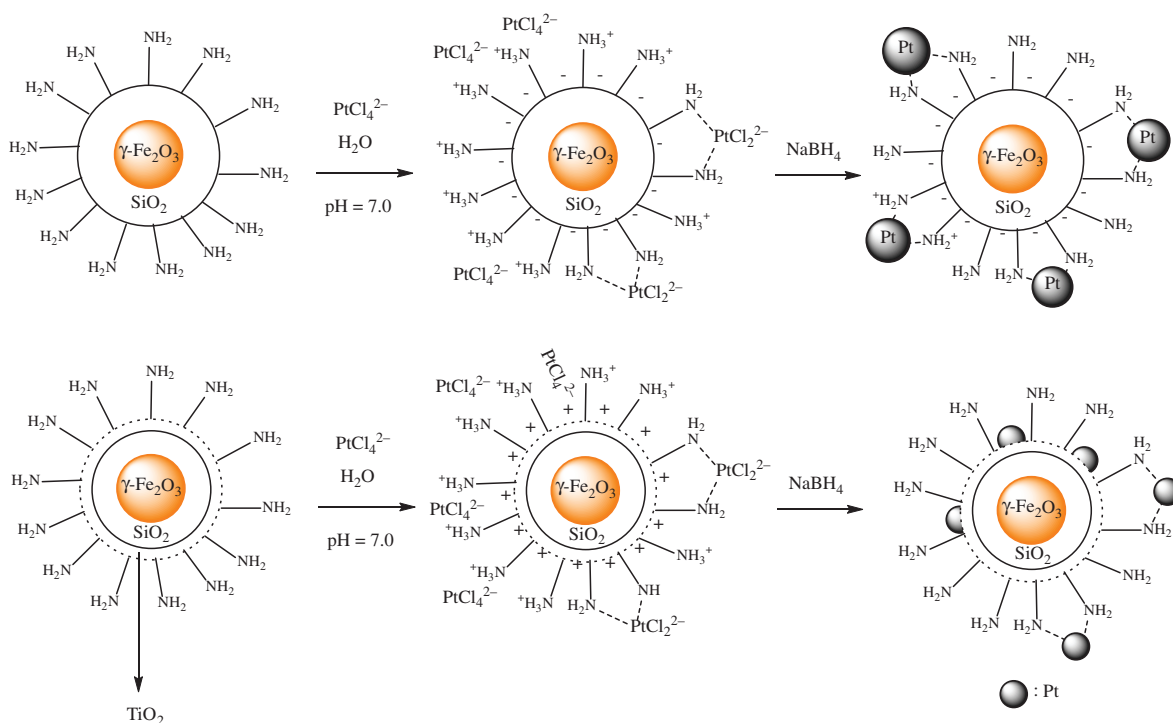
Scheme 2: Scheme of metal precursor interaction with FS and FST material.

metal precursor with the TiO_2 shell and $-NH_2$ groups and result in high Pt retention compared to that of the FS-Pt(x) catalysts.

Table 1 presents the results obtained for S_{BET} calculated from the N_2 adsorption-desorption isotherms at 77 K (Fig. S1). The FS and FST supports show isotherms typical of type II materials and S_{BET} values of 20 m^2/g. After Pt deposition on the FS and FST supports, the catalysts yield similar S_{BET} values to those of the supports, allowing the conclusion that the reduction of Pt^{2+} to Pt with $NaBH_4$ does not cause porosity in the SiO_2 or TiO_2 shells.

Figure 2 illustrates the XRD patterns of the synthesized materials. All systems show the diffraction peaks characteristic of an inverse spinel for γ-Fe_2O_3 (JCPDS 39-1346), as derived from the transformation of the Fe_3O_4-core to Fe_2O_3 during calcination [38]. For the FS-Pt(1) and FS-Pt(5) catalysts, only a diffraction peak at $2\theta = 39°$ is detected, corresponding to the metallic Pt (JCPDS 04-0802) on the surface. In the FST-Pt(x) systems, no diffraction signals are detected for TiO_2 (anatase or rutile) since the TiO_2 shell must be forming crystals with particle diameters below the XRD detection limit (<5.0 nm).

The FST-Pt(1) catalyst presents no diffractions attributed to Pt species (metallic Pt or PtO_x), while the FST-Pt(5) catalyst pattern reveals the presence of metallic Pt, as shown in Fig. 2. The above assumes that the average particle size for metallic Pt in the catalysts follows the order, FST-Pt(1) < 5.0 nm < FST-Pt(5).

The high-resolution transmission electron microscopy (HR-TEM) characterization is presented in Fig. 3 for the image sequence obtained at each step of the catalyst synthesis; the Fe_3O_4-core characterization is shown in the Supplementary Material (Fig. S2). Figure 3a and b reveal the CSNs where the γ-Fe_2O_3 core is covered by a layer of SiO_2 close to 50 nm thick. Figure 3b details the FST system, also obtained with the CSN structure as well as a second TiO_2 shell on the surface, with an irregular coating reaching an average thickness between 14 and 16 nm. For the catalysts supported on FS and FST (Table 1), in general, the average diameter of the γ-Fe_2O_3 core and the thickness diameters of the SiO_2 and TiO_2 shells do not vary during Pt deposition on the surface. For the FS-Pt(1) and FS-Pt(5) catalysts (Fig. 3e and g), increases in the metal crystal size are observed with increments of Pt loading.

During the impregnation-reduction, the FS-Pt(1) system presents an average particle size of 3.6 nm. When the procedure is repeated in successive steps, a uniform increase in Pt size is observed until reaching
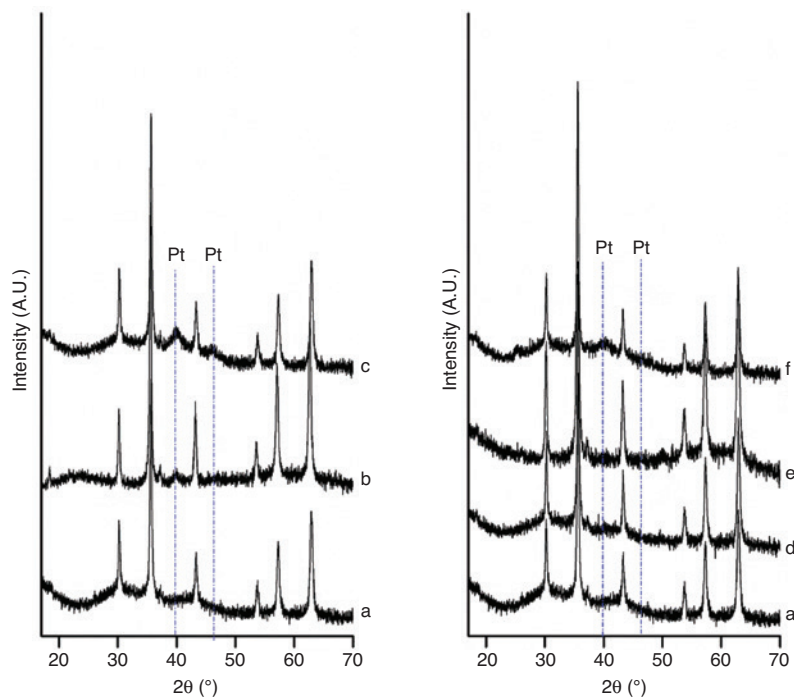
Fig. 2: XRD profiles for the as synthetized materials. (a) FS, (b) FS-Pt(1), (c) FS-Pt(5), (d) FST, (e) FST-Pt(1) and (f) FST-Pt(5).

a narrow distribution of metal particle diameters approximately 5.4 nm for the FS-Pt(5) system. The above is in line with the results obtained by ICP-OES and XRD for both catalysts. To confirm the effectiveness of the method, the effect of the preparation method was analyzed by placing the FS material functionalized with APTMS into contact with a solution of the $PtCl_4^{2-}$ precursor to obtain a catalyst with a metal loading of 5 wt% in a single step.

The HR-TEM results are shown in the Supplementary Material (Fig. S3), where a heterogeneous distribution of aggregates on the surface, reaching an average value of 13.4 ± 4.9 nm, is observed. The catalyst preparation method by successive impregnation-reduction allows for the generation of Pt clusters with a narrow particle size distribution, as controlled by the number of deposition cycles of the active phase.

Figure 3f and h display the FST-Pt(1) and FST-Pt(5) structures, where the Pt size distribution follows the same trend as that of the FS-Pt(x) systems (Table 1). However, the active phase presents a more homogeneous particle diameter distribution than do the FS-Pt(x) catalysts. The above is attributed to the stabilizing capacity of TiO_2 promoting a better dispersion of the $PtCl_4^{2-}$ precursor during metal deposition on the CSN surface (Scheme 2). The chemical microanalysis of FS and FST CNNs structure is examination for STEM-XEDS analysis in Fig. 3c and d. In order to confirm the composition of CNN structure, a diametral line-scan analysis was made. The FS system present only Fe and Si line-scans profiles also confirming the symmetry in morphology of structure. The FST materials present additionally the EDX signals of the respective TiO_2 on the CNN surface. Table 1 details the dispersion of the metal on the catalysts; a general trend is observed for the FS-Pt(x) and FST-Pt(x) catalysts, whereby an increase in dispersion follows a decrease in the average particle size.

The magnetic properties analysis confirmed that all FS-Pt(x) and FST-Pt(x) catalysts exhibited ferromagnetic properties (Fig. S4). The magnetic saturation (M_s) value of the materials FS is lower than that FST (Table 2), which may be attributed to the cover or FS by TiO_2 as a second shell. The incorporation of Pt do not modified the γ-Fe_2O_3 core magnetic properties [40]. Although FS-Pt(x) and FST-Pt(x) catalysts showed the relative low value of M_s, the values of 30–40 emu/g was enough for the efficiently removal (below 2 min) of those micro-sized particles, which reflected the ability of these catalysts to respond to an external magnetic field and quickly separated from the liquid phase [41].
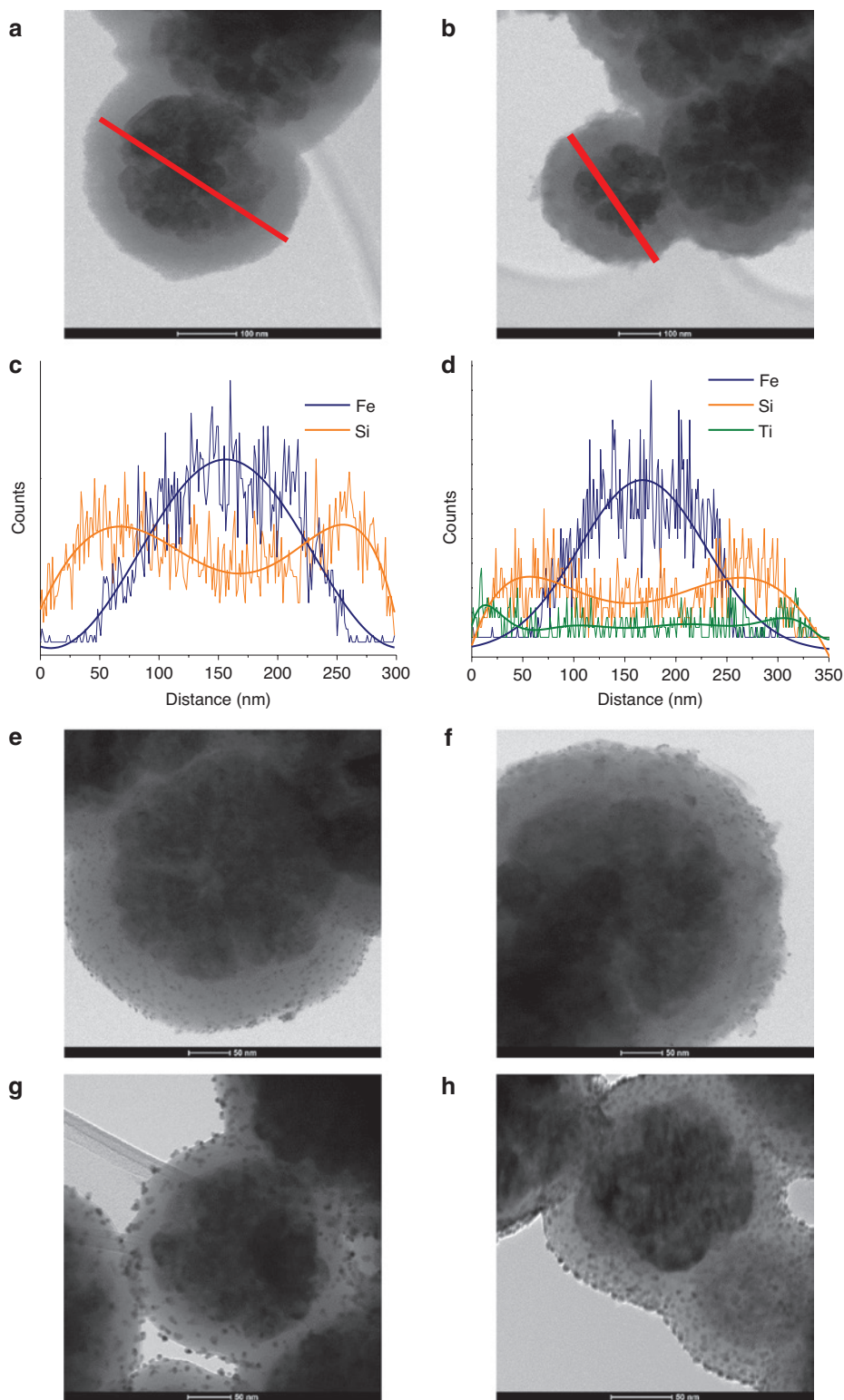
Fig. 3: HR-TEM micrographs and STEM-XEDS elemental mapping of the as prepared supports and catalysts. (a) FS, (b) FST, (c) FS elemental mapping, (d) FST elemental mapping, (e) FS-Pt(1), (f) FST-Pt(1), (f) FST-Pt(5), (g) FS-Pt(5) and (h) FST-Pt(5).

The catalysts were analyzed by X-ray photoelectron spectroscopy (XPS), and a summary of the obtained results is shown in Table 2. For all systems, the binding energy (BE) ranges for Pt $4f_{7/2}$, Si 2s, and Ti $2p_{3/2}$ were examined. All systems exhibit BE values for Si 2s and Ti $2p_{3/2}$ on the order of 101.4 eV and 458.5 eV, respectively,

Table 2: VSM and XPS characterization for the as synthetized supports and catalysts based on FS and FST materials.

Material	M_r (emu/g)	Binding energy (eV)		
		Pt 4f$_{5/2}$	Ti 2p$_{3/2}$	Si 1s
FS	40.3	–	–	103.4
FS-Pt(1)	42.9	70.9	–	103.5
FS-Pt(5)	43.2	71.4	–	103.3
FST	33.7	–	458.5	103.2
FST-Pt(1)	33.0	72.0	458.7	103.2
FST-Pt(5)	33.5	72.0 (74.3)	458.4	103.2

In brackets the contribution of Pt$^{\delta+}$ species for deconvolution of Pt 4f$_{7/2}$ signal.

and are related to Si^{4+} and Ti^{4+} species forming SiO$_2$ and TiO$_2$ oxides. For the FS-Pt(x) and FST-Pt(x) catalysts, the XPS spectra are shown in Supplementary Material (Fig. S5 a–d). In the case of the FS-Pt(1) and FS-Pt(5) catalysts, only Pt is detected in the metallic state at BE of 70.9 eV and 71.4 eV, respectively. However, the FST-Pt(1) and FST-Pt(5) systems reveal a BE shift to 72.0–71.5 eV for the metallic Pt species, and a second contribution of Pt$^{\delta+}$ species is also detected is also detected at BE: 74.3 eV (see Table 2). The above indicates the strong Pt-TiO$_2$ surface interaction that has been reported by some authors as having a Pt$^{\delta+}$ signal appearing at a BE lower than that of metallic Pt [35, 42–44].

Effects of the shell and average Pt particle size on CIN hydrogenation

Figure 4 shows the curves for the product yield and distribution over time for CIN hydrogenation via the FS-Pt(x) and FST-Pt(x) catalysts. The conversion curves follow pseudo-first-order kinetics with respect to the conversion of CIN, as shown in Fig. 4a and d. Table 3 contains a summary of the calculated kinetic parameters. No by-products from the phenyl hydrogenation of CIN, HCIN, COL and/or HCOL, hydrodeoxygenation to produce 1-phenyl-propane and/or trans-1-phenyl-1-propene, or hemiacetal or acetal formation were detected among the reaction products. Furthermore, blank tests were performed in the absence of a catalyst with the FS and FST supports, no CIN conversion at 1440 min (24 h) of reaction is observed. The FS-supported systems exhibit differences in their conversion rates, with the FS-Pt(5) system reaching the maximum conversion at 360 min of reaction and with the FS-Pt(1) system reaching the maximum at 600 min. However, the rate constants (see Table 3) present values within the same order of magnitude.

This behavior agrees with the results reported by Durndell et al. since the constants are normalized by the surface Pt content (estimated from the metal dispersion data by TEM and XPS) and do not show a dependence of the reaction rate on metal particle size. The product distributions are shown in Fig. 4b and c. The continuous production of COL in the FS-Pt(1) and FS-Pt(5) systems reaches maximum selectivity values of 49 % and 90 % at 600 and 420 min, respectively. The above result agrees with the TEM and XRD results, where the FS-Pt(5) catalyst shows metal particle size values favoring C=O adsorption on the surface of the active phase [28, 30].

The FST-Pt(x) systems garner lower hydrogenation rates of CIN and selectivities for COL production than those detected for the FS-Pt(x) catalysts. Although FST-Pt(1) and FST-Pt(5) proceed with pseudo-rate constants of ~19 min^{-1}g$_{Ptsup}$$^{-1}$, the transformation rate of the FST-Pt(1) system reaches the maximum conversion at 1440 min (24 h) of reaction with only 4 % selectivity for COL. Figure 6e indicates that the COL production goes through a maximum at the beginning of the reaction and then decreases systematically with time yielding HCOL as the main product. The above is attributed to the particle size of this catalyst. Several authors have reported decreases in the reaction rate and selectivity towards semi-hydrogenated products for particle sizes below 3.0 nm [27–30].

The catalytic performance of the FST-Pt(5) system reaches the maximum conversion at 600 min with a selectivity of 66 % to COL production. The product distribution profile (Fig. 4f) indicates that the COL
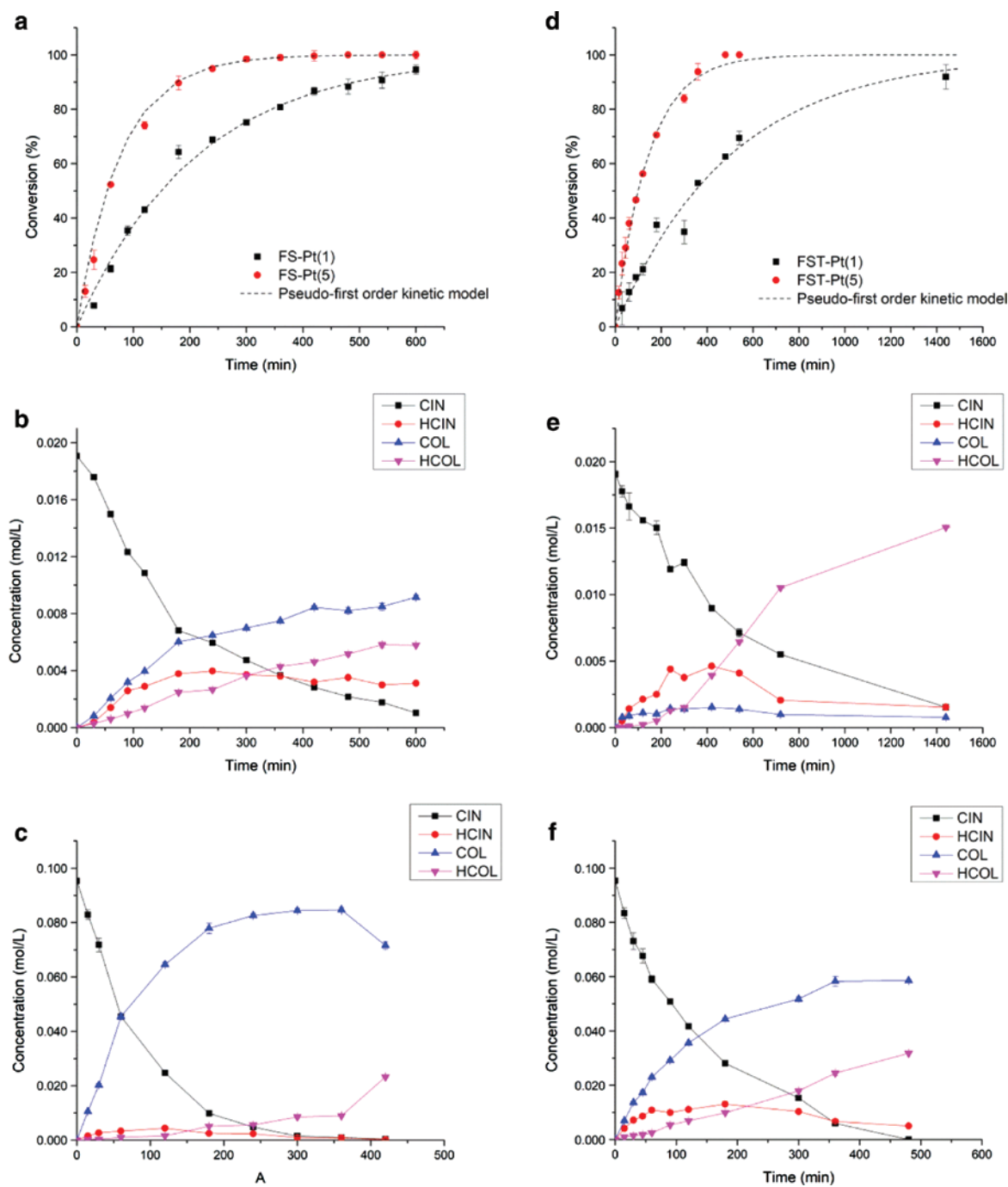
Fig. 4: Activity curves based on CIN conversion and products distribution for FS-Pt(x) and FST-Pt(x) catalysts. (a) Conversion curve for FS-Pt(x) catalysts, (b) products distribution for FS-Pt(1), (c) products distribution for FS-Pt(5), (d) conversion curve for FST-Pt(x) catalysts, (e) products distribution for FST-Pt(1) and (f) products distribution for FST-Pt(5).

concentration increases with time and that HCOL production primarily derives from the hydrogenation of HCIN.

By comparing the FS-Pt(5) and FST-Pt(5) systems, an increase in selectivity for the COL product is observed for the FS-Pt(5) system. Despite having similar metal particle sizes, the FST support surface could promote a competitive C=O adsorption on the TiO_2 surface, as reported by Wu et al. [45], decreasing the hydrogenation rate of CIN and the COL yield.

Table 3: Catalytic data for CIN hydrogenation over FS-Pt(x) and FST-Pt(x) catalysts.

Catalyst	X (%)	k (min^{-1}g$_{Pt(sup)}^{-1}$)^a			S (%)
			HCIN	COL	HCOL
FS-Pt(1)	88.6	49.4	17.3	50.7	32.0
FS-Pt(5)^b	100	47.2	1.0	90.0	9.0
FST-Pt(1)	57.4	19.6	34.3	11.7	54.0
FST-Pt(5)	100	18.3	5.2	61.5	33.3

The conversion levels determinate at 480 min of reaction and the selectivity was measured at the maximum level of conversion.
^{a}Normalizated by XPS data and dispersion values, ^{b}measured at 420 min because at this time the conversion level was 100 %.

Study of the SMSI effect on the production of COL

Regarding the results for the FST-Pt(x) systems, the FST-Pt(1) catalyst is not selective to COL production while the FST-Pt(5) system reaches a selectivity of 66 % to the product of interest. Because of this, the effect of reduction in the FST-Pt(5) catalyst system at 773 K was studied to promote the SMSI effect. Figure 5 shows the HR-TEM characterization of the (FST-Pt(5)-red) post-reduction catalyst revealing a change in the core morphology from a core-shell to an egg-shell structure; this shift is attributed to the reduction of γ-Fe$_2$O$_3$ to a mixture of metallic Fe and FeO$_x$ species, as shown by the XRD and TPR characterization in the Supplementary Material (Fig. S5).

Despite the change in core structure, the SiO$_2$@TiO$_2$ multi-shell retains its morphology after reduction. However, the magnetic susceptibility undergoes a change going from M$_r$ = 33.0 emu/g for the FST-Pt(5) system to M$_r$ = 68.1 emu/g for the FST-Pt(5)-red system and is attributed to the presence of metallic Fe after reduction. The metal particle size distribution for the FST-Pt(5)-red system increases up to values 7.9 ± 1.1 nm and is assigned to Pt sintering during reduction. The XPS characterization after reduction indicates the contributions of the metallic Pt species at BE = 73.4 eV and Pt$^{\delta+}$ at BE = 72.4 eV, with the latter attributed to the presence of TiO$_{2-x}$ species around the metal particles [45, 46], as shown in Table 2.

The activity curves and product distribution curves for CIN hydrogenation on the FST-Pt(5) and FST-Pt(5)-red catalysts are shown in Fig. 6. As with previous tests, the catalytic activity was only performed with the FST support reduced at 773 K where no catalytic activity had been detected at 1140 min (24 h), ruling out a reduced core effect on the catalytic performance. Based on the above, it may be assumed that during reduction, the SiO$_2$@TiO$_2$ multi-shell does not allow access of the substrate to the core, in line with S$_{BET}$ results included in the Supplementary Material (Fig. S5).

The activity curves for the FST-Pt(5)-red system show conversion profiles over time following pseudo-first-order kinetics with respect to CIN consumption, similar to those of FST-Pt(5) (see Fig. 6a). However, these
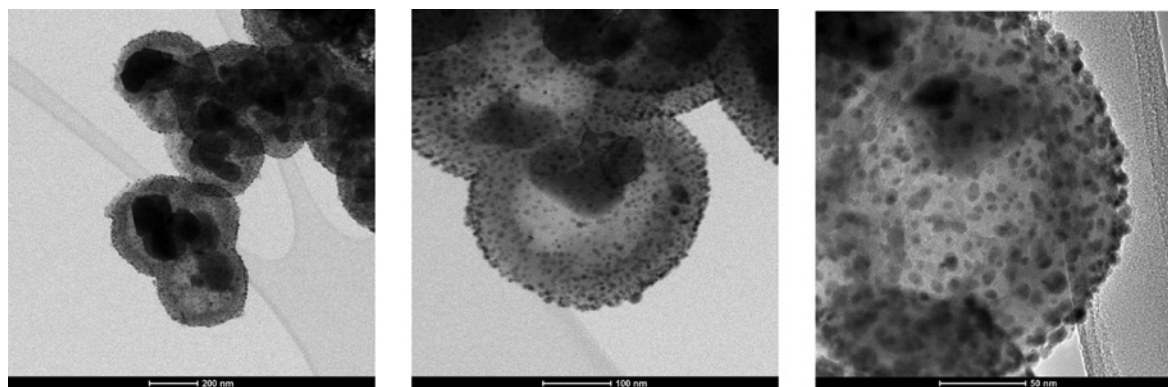

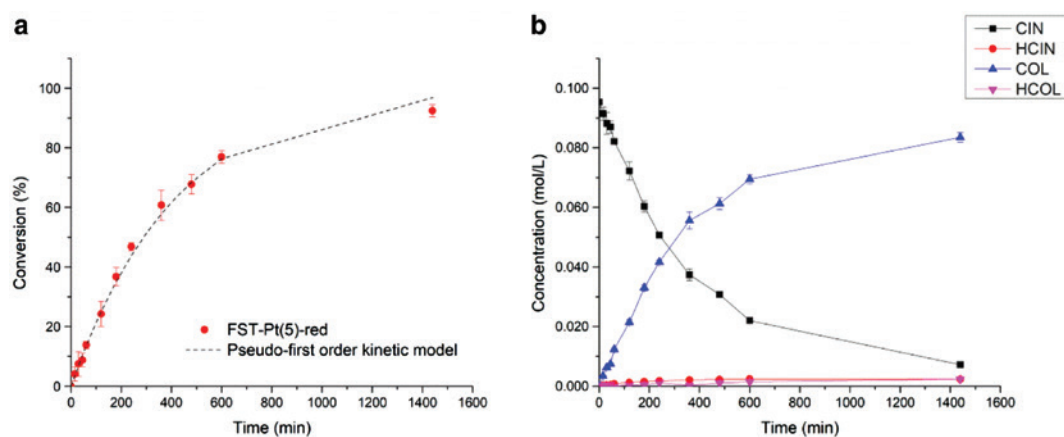**Fig. 5:** HR-TEM micrographs of FST-Pt(5)-red catalyst.

Fig. 6: Activity curves based on CIN conversion and products distribution for FST-Pt(5)-red catalyst. (a) conversion curve and (b) products distribution.

activity curves present slower conversions over time; the FST-Pt(5)-red system reaches the maximum conversion at 1440 min (24 h), while the FST-Pt(5) system reaches it at 600 min. Furthermore, compared to that of the FST-Pt(5) system, a significant increase in selectivity is observed, reaching 95 % of COL production at 90 min and remaining constant in time until obtaining the maximum conversion (Fig. 6b). The increase in selectivity can be explained as a function of the combined effects of the increase in metal particle size and the SMSI effect, as shown in Scheme 3. The FST-Pt(5)-red catalyst presents an increase in particle size after reduction (HR-TEM) and the formation of SMSI is further supported by XPS measurements (Fig S4.e). The BE of Pt^0 $4f_{7/2}$ shifts from 72.0 to 71.3 eV with reduction treatment. This shift can not be related to changes of Pt particle size or oxidation state but may be attributed to donating of electron from TiO_x to Pt due to the formation of SMSI. The presence of Pt-TiO_{2-x} species (XPS) favoring the selective hydrogenation of the C=O group. The average Pt size discourages the coplanar adsorption of the CIN molecule at the active site, and the coverage with TiO_{2-x} species during reduction favors the linear adsorption of the C=O group on the surface of the active phase.
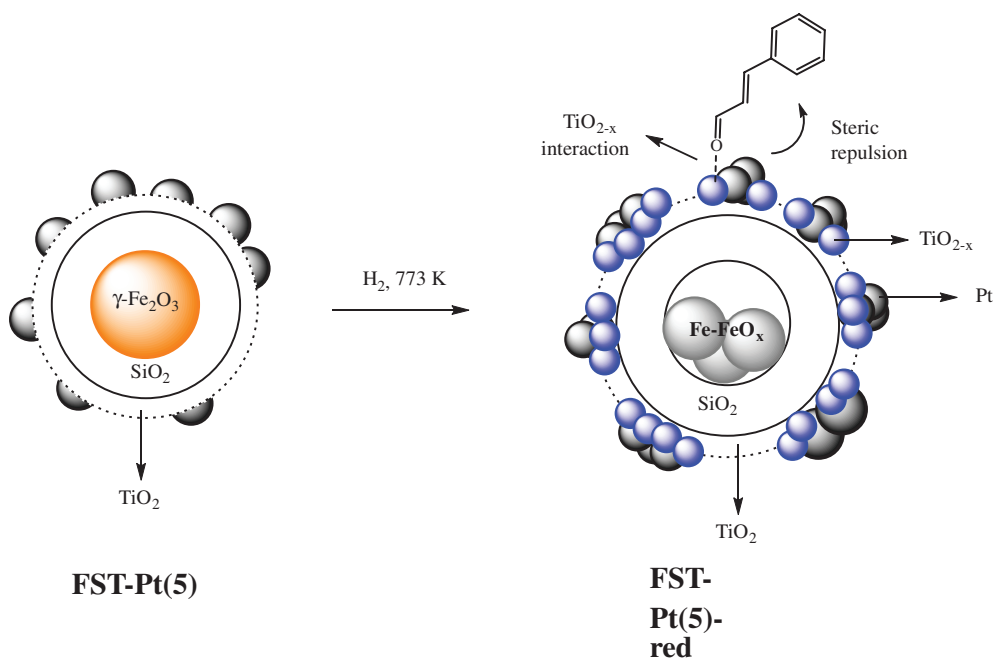
Scheme 3: Model of SMSI effect and Pt NPs growth after FST-Pt(5) reduction treatment.

Recycling studies

The catalytic activity tests indicate that the most selective systems are FS-Pt(5) and FST-Pt(5)-red, with over 90 % selectivity in the production of COL. Catalyst separation from the reaction medium was performed to measure the activity of the reaction mixture in the absence of a catalyst and to check whether leaching of the active phase occurred during the operating time of the catalysts.

Figure 7 presents the activity curves for the reactions in the presence of the catalysts and for the reaction crudes separated at 120 min. For the filtered FS-Pt(5) catalyst, non-variation in the conversion is observed over time (Fig. 7a).

The above is attributed to the no-leaching of Pt NPs to the liquid phase. For the FST-Pt(5)-red system, no catalytic activity attributed to the stabilization of the active phase on the FST support surface by the SMSI effect is observed (Fig. 7b). Therefore, recycling tests were performed for FS-Pt(5) and FST-Pt(5)-red system, with the results displayed in Fig. 7c and d. The FS-Pt(5) catalyst shows a sustained activity and selectivity in the production of COL until the third operating cycle, where a non-decrease in activity is observed, reaching a maximum conversion of at 300 min of operation.

The FST-Pt(5)-red catalyst shows the same activity and selectivity profile in the production of COL until the third operating cycle, where a decrease in activity is observed, reaching a maximum conversion of 78 % at 1440 min (24 h) of operation. The HR-TEM characterization of the catalyst after the third cycle (Fig. S6) demonstrates that the catalyst does not change its morphology or particle size distribution during the operating
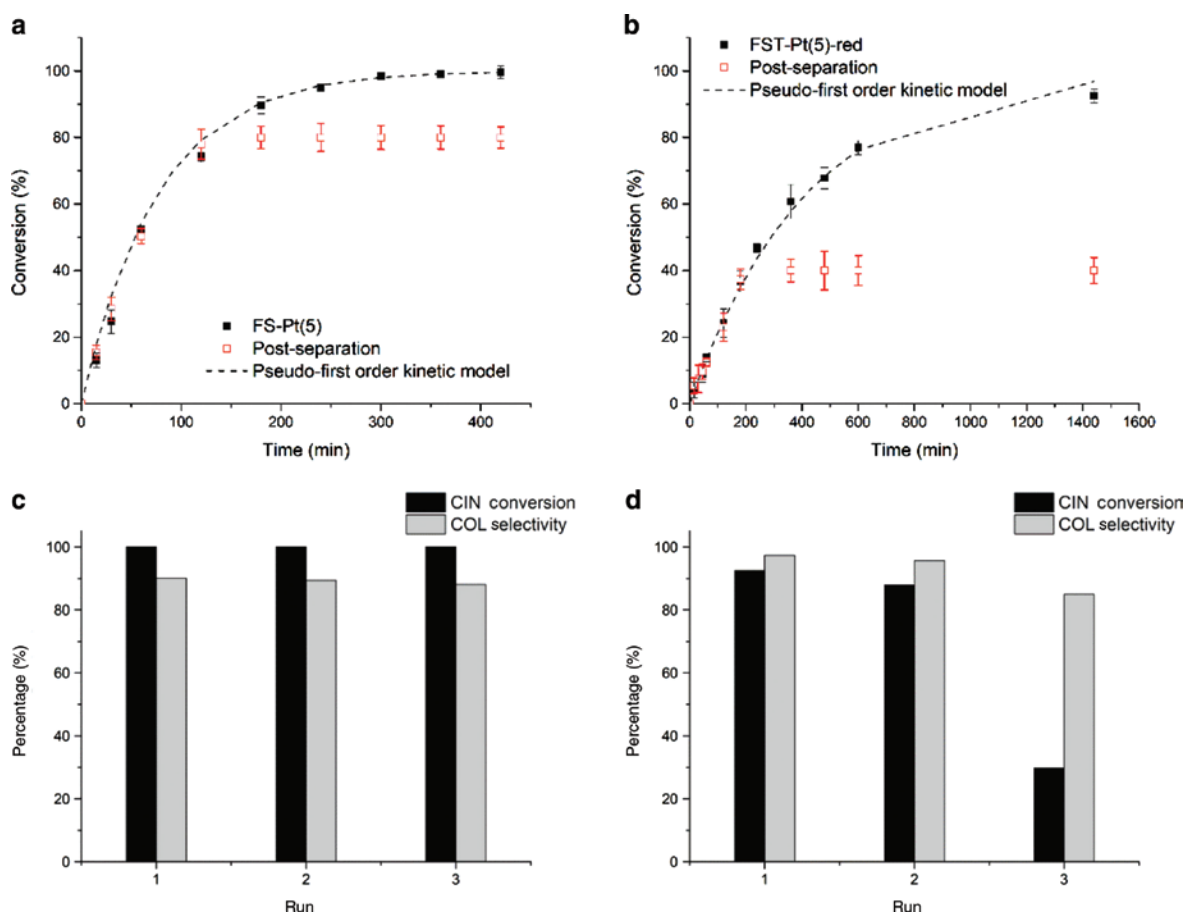

Fig. 7: Stability tests for the FS-Pt(5) and FST-Pt(5)-red catalysts. (a) FS-Pt(5) conversion curve for the reaction medium at 120 min post-hydrogenation and (b) FST-Pt(5)-red conversion curve for the reaction medium at 120 min post-hydrogenation, (c) recycles for the FS-Pt(5) catalyst and (d) recycles for the FST-Pt(5)-red catalyst.

cycles. However, the ICP-OES measurement for the supernatant in the supernatant of the third cycle, Pt is detected in the liquid phase corresponding to 28 % leachate.

Conclusions

The effects of the nature of the support, metal particle size, and reduction in Pt catalysts supported on core-shell structures were studied. Material design allowed for the construction of a magnetic core (γ-Fe$_2$O$_3$) to separate the systems by simple magnetization of the reaction medium. The size effect was controlled with catalyst metal loading – obtained by incorporating the metal with successive impregnations – in systems with 5 wt% Pt, thereby allowing for catalysts with narrow metal particle size distributions. The effect of Pt crystal size is that catalysts with a metal loading of 5 wt% were more active and selective in the hydrogenation of cinnamaldehyde to produce cinnamyl alcohol since catalysts with average particle sizes of 5.4 and 4.9 nm were obtained for γ-Fe$_2$O$_3$@SiO$_2$-5%Pt and γ-Fe$_2$O$_3$@SiO$_2$@TiO$_2$-5%Pt, respectively. The above confirms the information reported in the literature regarding the size effect of the active phase towards the hydrogenation selectivity for cinnamaldehyde. The γ-Fe$_2$O$_3$@SiO$_2$-5%Pt catalyst was more active and selective than the γ-Fe$_2$O$_3$@SiO$_2$@TiO$_2$-5%Pt catalyst thanks to the average particle size obtained for catalysts supported on the SiO$_2$ shell. However, when the γ-Fe$_2$O$_3$@SiO$_2$@TiO$_2$-5%Pt system was subjected to reduction in H$_2$ at 773 K, an increase in the selectivity for cinnamyl alcohol production of 95 % of the maximum conversion was achieved due to the combined effects of the average particle size and the SMSI effect during reduction treatment. Finally, γ-Fe$_2$O$_3$@SiO$_2$-5%Pt system showed a higher operational stability than γ-Fe$_2$O$_3$@SiO$_2$@TiO$_2$-5%Pt because in a recycling experiment the catalyst system γ-Fe$_2$O$_3$@SiO$_2$-5%Pt was quantitatively recovered for third times without any loss in activity and selectivity.

References

[1] D. K. Yi, S. S. Nanda, K. Kim, S. Tamil Selvan. *J. Mater. Chem. B* **5**, 9429 (2017).
[2] Y. P. Pang, J. Wang, Z. G. Zhou, T. Yuan, J. H. Yang, D. L. Sun, S. Y. Zheng. *J. Alloys Compd.* **735**, 833 (2018).
[3] A. M. El-Toni, M. A. Habila, J. P. Labis, Z. A. Alothman, M. Alhoshan, A. A. Elzatahry, F. Zhang. *Nanoscale* **8**, 2510 (2016).
[4] M. B. Gawande, A. Goswami, T. Asefa, H. Guo, A. V. Biradar, D.-L. Peng, R. Zboril, R. S. Varma. *Chem Soc. Rev.* **44**, 7540 (2015).
[5] R. Ghosh Chaudhuri, S. Paria. *Chem. Rev.* **112**, 2373 (2012).
[6] Y. Long, K. Liang, J. Niu, B. Yuan, J. Ma. *Dalton Trans.* **44**, 8660 (2015).
[7] X. Lan, N. Huang, J. Wang, T. Wang. *Catal. Sci. Technol.* **7**, 2601 (2017).
[8] T. Urayama, T. Mitsudome, Z. Maeno, T. Mizugaki, K. Jitsukawa, K. Kaneda. *Chem. – Eur. J.* **22**, 17962 (2016).
[9] I. Nongwe, V. Ravat, R. Meijboom, N. J. Coville. *Appl. Catal. A* **517**, 30 (2016).
[10] X. Lan, T. Wang, X. Li, N. Huang, J. Wang. *Catal. Sci. Technol.* **6**, 7703 (2016).
[11] S. Huang, N. Yang, M. Huo, Y. Sun, Y. Zhu. *Nanoscale* **8**, 6451 (2016).
[12] X. Qi, M. R. Axet, K. Philippot, P. Lecante, P. Serp. *Dalton Trans.* **43**, 9283 (2014).
[13] T. Mitsudome, M. Matoba, T. Mizugaki, K. Jitsukawa, K. Kaneda. *Chem. – Eur. J.* **19**, 5255 (2013).
[14] K. Taniya, C. H. Yu, S. C. Tsang, Y. Ichihashi, S. Nishiyama. *Catal. Comm.* **14**, 6 (2011).
[15] K. Kaneda, T. Mitsudome. *Chem. Rec.* **17**, 4 (2016).
[16] P. Gallezot, D. Richard. *Catal. Rev.: Sci. Eng.* **40**, 81 (1998).
[17] S. J. Tauster, S. C. Fung. *J. Catal.* **55**, 29 (1978).

[18] D. E. Resasco, R. S. Weber, S. Sakellson, M. McMillan, G. L. Haller. *J. Phys. Chem.* **92**, 189 (1988).

[19] J. Zhao, J. Ni, J. Xu, J. Xu, J. Cen, X. Li. *Catal. Comm.* **54**, 72 (2014).

[20] W. S. Putro, T. Kojima, T. Hara, N. Ichikuni, S. Shimazu. *Catal. Sci. Technol.* **7**, 3637 (2017).

[21] Y. Zhang, S. Zhang, X. Pan, M. Bao, J. Huang, W. Shen. *Catal. Lett.* **147**, 102 (2017).

[22] M. G. Prakash, R. Mahalakshmy, K. R. Krishnamurthy, B. Viswanathan. *Catal. Sci. Technol.* **5**, 3313 (2015).

[23] H. Rojas, J. J. Martínez, S. Mancípe, G. Borda, P. Reyes. *React. Kinet. Mech. Catal.* **106**, 445 (2012).

[24] C. M. Piqueras, V. Puccia, D. A. Vega, M. A. Volpe. *Appl. Catal. B* **185**, 265 (2016).

[25] H. Chen, D. A. Cullen, J. Z. Larese. *J. Phys. Chem. C* **119**, 28885 (2015).

[26] F. Jiang, J. Cai, B. Liu, Y. Xu, X. Liu. *RSC Adv.* **6**, 75541 (2016).

[27] L. J. Durndell, C. M. A. Parlett, N. S. Hondow, M. A. Isaacs, K. Wilson, A. F. Lee. *Sci. Rep.* **5**, 9425 (2015).

[28] C. Vriamont, T. Haynes, E. McCague-Murphy, F. Pennetreau, O. Riant, S. Hermans. *J. Catal.* **329**, 389 (2015).

[29] A. J. Plomp, H. Vuori, A. O. I. Krause, K. P. de Jong, J. H. Bitter. *Appl. Catal. A* **351**, 9 (2008).

[30] A. K. Prashar, S. Mayadevi, R. Nandini Devi. *Catal. Comm.* **28**, 42 (2012).

[31] F. Leng, I. C. Gerber, M. R. Axet, P. Serp. *C. R. Chim.* **21**, 346 (2018).

[32] M. A. Habila, Z. A. Alothman, A. M. El-Toni, J. P. Labis, M. Soylak. *Talanta* **154**, 539 (2016).

[33] Y. Zhang, Y. Xie, A. Tang, Y. Zhou, J. Ouyang, H. Yang. *Ind. Eng. Chem. Res.* **53**, 5507 (2014).

[34] R. Morales, C. H. Campos, J. L. G. Fierro, M. A. Fraga, G. Pecchi. *Catal. Today* **310**, 59 (2018).

[35] S. Ali Ansari, M. Mansoob Khan, M. Omaish Ansari, M. Hwan Cho. *Ceram. Int.* **41**, 9131 (2015).

[36] D. Jain, M. Mishra, A. Rani. *Fuel Process. Technol.* **95**, 119 (2012).

[37] D. Niu, Y. Li, X. Qiao, L. Li, W. Zhao, H. Chen, Q. Zhao, Z. Ma, J. Shi. *Chem. Comm.* **37**, 4463 (2008).

[38] T. Guo, W. Jiang, Y. Ruan, L. Dong, H. Liu, H. Li, W. Zhu, H. Li. *Colloids Surf. A* **537**, 243 (2018).

[39] Y. Yang, J. Pan, N. Zheng, X. Liu, J. Zhang. *Appl. Catal.* **61**, 75 (1990).

[40] Z. Teng, X. Su, G. Chen, C. Tian, H. Li, L. Ai, G. Lu. *Colloids Surf. A* **402**, 60 (2012).

[41] Z. Qi, T. P. Joshi, R. Liu, H. Liu, J. Qu. *J. Hazard. Mater.* **329**, 193 (2017).

[42] C. H. Campos, C. C. Torres, A. B. Dongil, D. Ruiz, J. L. G. Fierro, P. Reyes. *Catal. Today* **235**, 226 (2014).

[43] X. Zhao, J. Zhu, L. Liang, J. Liao, C. Liu, W. Xing. *J. Mater. Chem.* **22**, 19718 (2012).

[44] L. Yu, Y. Shao, D. Li. *Appl. Catal. B* **204**, 216 (2017).

[45] Q. Wu, C. Zhang, B. Zhang, X. Li, Z. Ying, T. Liu, W. Lin, Y. Yu, H. Cheng, F. Zhao. *J. Colloid Interface Sci.* **463**, 75 (2016).

[46] C.-J. Pan, M.-C. Tsai, W.-N. Su, J. Rick, N. G. Akalework, A. K. Agegnehu, S.-Y. Cheng, B.-J. Hwang. *J. Taiwan Inst. Chem. Eng.* **74**, 154 (2017).